Journal of Nuclear Materials 189 (1992) 318–332
North-Holland

journal of nuclear materials

Precipitate evolution in the Zircaloy-4 oxide layer

D. Pêcheur, F. Lefebvre, A.T. Motta [1] and C. Lemaignan
CEA / CEN-Grenoble, DTP / SECC, 85X, 38041 Grenoble Cedex, France

J.F. Wadier,
Cézus-Centre de Recherches de Ugine, 73400 Ugine, France

Received 13 February 1992; accepted 7 April 1992

A study by transmission electron microscopy has been made of the incorporation and oxidation of intermetallic precipitates $Zr(Cr,Fe)_2$ into the uniform oxide layer of Zircaloy-4. Oxide thicknesses of 1, 4 and 14 μm were studied. The main results are: (i) most of the precipitates are incorporated unoxidized into the oxide layer and are later oxidized. (ii) iron concentration evolves significantly during oxidation, especially before the transition, generally segregating to the precipitate–matrix interface, occasionally precipitating as metallic iron, before being dissolved in the matrix. In order to understand the behaviour of fuel cladding in a reactor environment, the same approach was then realized on ion irradiated samples. In this case, the studied oxide thickness was 1 μm. The $Zr(Fe,Cr)_2$ precipitates made amorphous by ion irradiation appear to behave as the original intermetallic precipitates. However, the iron redissolution seems to be delayed in the ion irradiated precipitates. The behavior of the precipitates during oxidation is discussed in the light of previous work and possible consequences for the oxidation process are considered.

1. Introduction

Corrosion of zirconium alloys is one of the main limitations to the use of high burnup fuel rods in light water reactors (LWR) [1].

Many research teams have studied the oxidation of zirconium alloys, pointing out several factors controlling their oxidation. This oxidation is usually described in two steps, with a transition between a cubic and a linear oxidation rate. It was found that the size, chemical composition and distribution of the intermetallic precipitates $Zr(Cr,Fe)_2$ in Zircaloy-2 and -4 and $Zr_2(Fe,Ni)$ in Zircaloy-2 significantly alter the oxidation process by retarding or anticipating the transition of the oxidation process or by enhancing pre- and post-transition oxidation rates [2–6].

Few studies have been published, however, on the actual mechanisms of precipitate incorporation in the oxide layer [7,8]. In this work, an investigation by transmission electron microscopy (TEM) is made of the state of as-fabricated crystalline intermetallic precipitates when incorporated into the Zircaloy-4 oxide layer. Neutron irradiation and PWR conditions are known to increase the post transition oxidation rate [9]. Since neutron irradiation modifies significantly the oxidation behaviour of Zircaloy fuel cladding and, on the other hand, produces major microstructure evolutions such as precipitate amorphization and then dissolution [10,11], we have produced these irradiation induced damages and then studied their effect on oxidation. The incorporation into the Zircaloy-4 oxide layer of precipitates previously made amorphous by ion irradiation was then studied.

After reporting experimental results, the precipitate oxidation process is discussed and a comparison is made betwen the incorporation and oxidation of crystalline precipitates and of precipitates previously made amorphous by ion irradiation.

[1] Now at Department of Nuclear Engineering, The Pennsylvania State University, 231 Sacket Building, University Park, PA 16802, USA.

2. Experimental methods

2.1. Material

The material used for this work is standard Zircaloy-4 furnished by CEZUS of Ugine, France. Samples have been machined out of a plate (Zr–1.45 wt% Sn–0.21 wt% Fe–0.10 wt% Cr) fully recrystallized at 925 K for 3 h 20 min after cold rolling and then heat treated at 1055 K during 50 h. This last step was performed to increase precipitate size and thereby facilitate their observation.

2.2. Corrosion

Samples were oxidized in static autoclave exposure in 10.3 MPa steam, at 675 K for 3, 40 and 420 days. The measured weight gains for those times were 17, 57 and 207 mg dm^{-2} respectively, which correspond approximately to oxide thicknesses of 1, 4 and 14 μm.

2.3. TEM examination

After oxidation, samples were mechanically polished from the inner surface by hand grinding and then punched into 3 mm diameter samples. The oxide scale being protected by a varnish, the disc samples were then electropolished on the other side to remove the remaining base metal.

The last step was performed in an ion mill in order to control the section of the oxide layer to be observed: samples milled from one side allowed the study of the opposite side; samples milled from both sides allowed the observation of regions in between the metal–oxide interface and the oxide surface.

Observations were carried out in a JEOL 1200 EX

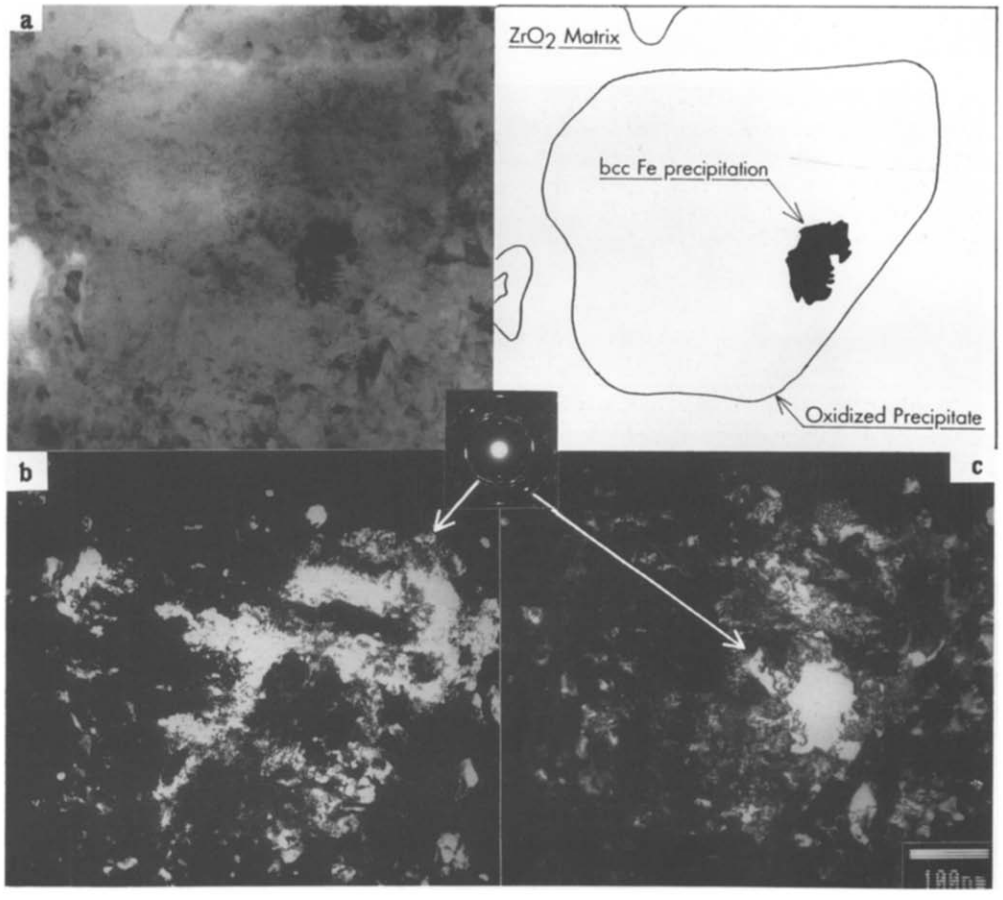

Fig. 1. (a) Microcrystalline oxidized precipitate located at the water–oxide interface of a 1 μm thick oxide layer. (b) Dark field of a few clusters of small tetragonal ZrO_2 crystallites. (c) Dark field of a ⟨110⟩ bcc iron agglomeration reflection.

scanning transmission electron microscope and chemical composition data was obtained by energy dispersive X-ray spectroscopy. The measured parameter was the Fe/Cr ratio.

2.4. Ion irradiation

Ion irradiation was chosen to simulate neutron irradiation because it can deliver large doses in short times [12], in reproducible conditions, and it has been previously shown to amorphize the intermetallic precipitates in Zircaloy [13].

1.5 MeV He^+ ion irradiations were performed in the Van de Graaff ion accelerator of the Centre d'Etudes Nucléaires de Grenoble. The current density was 0.5 $\mu A\ cm^{-2}$ and the irradiation temperature was 80 K. The temperature was measured with a thermocouple attached to the front surface of the specimen. With these experimental conditions, a damage level of 0.4 displacements per atom (dpa) was obtained at the sample surface after 16 hours of irradiation, as calculated by TRIM 86 [14].

The weight gain after a three day oxidation for the irradiated sample was 15 mg dm^{-2} corresponding to a layer thickness of 1 μm.

The heat treatment corresponding to the corrosion test (675 K for three days) could affect irradiated precipitate microstructure and chemical composition.

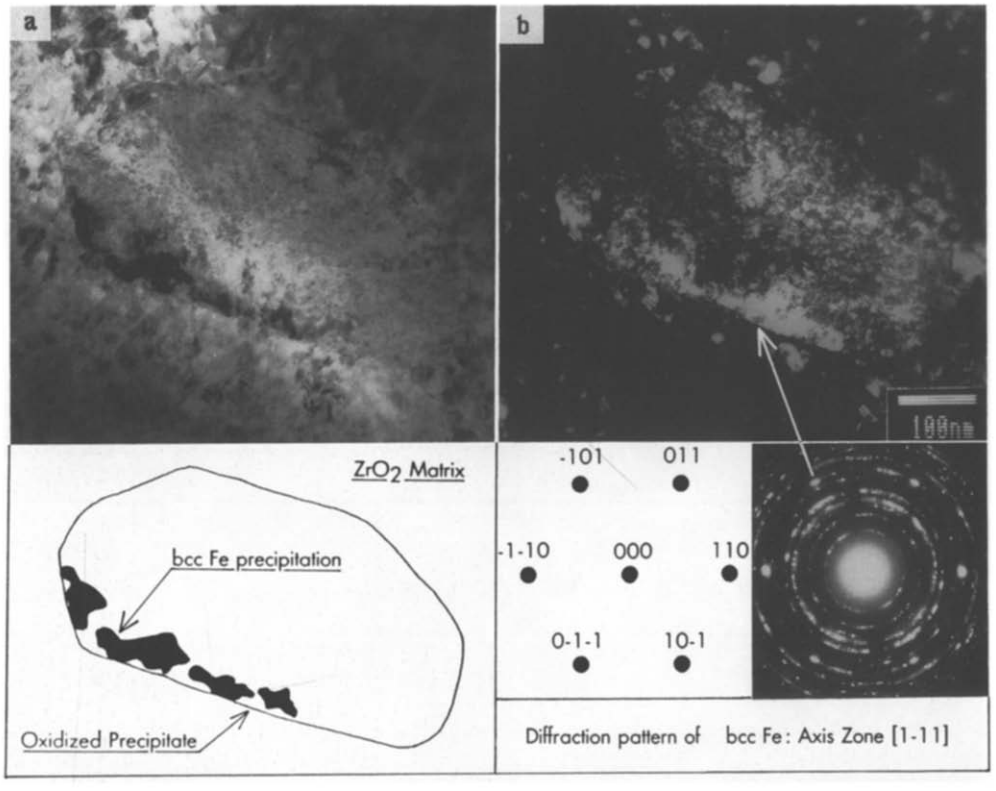

Fig. 2. (a) Microcrystalline oxidized precipitate located at the water–oxide interface of a 1 μm thick oxide layer. (b) Dark field of a ⟨110⟩ bcc iron agglomeration reflection and some of the adjacent tetragonal spot.

Accordingly, irradiated samples were held under these conditions in vacuum in order to separate the effects of thermal treatment on precipitate evolution from those due to oxidation. The only effect observed after the heat treatment was a slight depletion of iron in the amorphous precipitates: the Fe/Cr ratio decreases from the as-fabricated value of 1.7 at the middle of the precipitate to 1.5 near the edge. No recrystallization of the amorphous phase was observed during heat treatment, which is to be expected, since annealing studies show that amorphous precipitates only recrystallize after heat treatment at 875 K for 1 hour [15,16].

3. Experimental results on reference Zircaloy-4

3.1. Reference precipitate morphology

After the specific coarsening heat treatment, the Zircaloy-4 sheet used in this work has a grain size ranging between 20 and 130 μm. $Zr(Cr,Fe)_2$ precipitate structure and morphology in Zircaloy-4 have been extensively characterized elsewhere [17–19]: the C14 hcp or the C15 fcc Laves phases were found. In this work both structures have been also found, but no determination of relative quantities has been made. Precipitates in the present samples have a diameter between 0.15 and 0.8 μm, the average diameter being about 0.3 μm. Their Fe/Cr ratio (1.7) is independent of their size and crystalline structure.

3.2. Oxidation of $Zr(Fe,Cr)_2$ precipitates

3.2.1. 3 day oxidation: oxide thickness = 1 μm (before transition)

– At the water–oxide interface of the oxide layer, all precipitates are oxidized and their Fe/Cr ratio is decreased to less than 1. An oxidized precipitate is shown in fig. 1a, along with its diffraction pattern, showing tetragonal or cubic ZrO_2 which is present in the oxidized precipitate but not in the matrix. In this work, no distinction has been made between cubic and tetragonal ZrO_2 since their characteristic electron diffraction patterns are very similar. The oxidized precipitate morphology consists of small rod-shaped crystallites, a few nm in size, gathered into clusters of similar orientation. These clusters can be seen in fig. 1b, which is a dark field taken with one of the tetragonal/cubic spots. Chemical composition analysis of the precipitate shows that iron is segregated to the edges of the precipitates. In the larger precipitates (> 0.35 μm) such segregation results in precipitation of a new phase, identified as bcc iron, with a lattice parameter of 2.87 Å. In fig. 1c, a dark field of one of the ⟨110⟩ bcc iron spots is presented, the arrow shows the iron precipitation. Chemical analysis of those agglomerates shows a very high percentage of iron. Such an iron redistribution has already been reported by Ploc upon oxidation of Zr_3Fe intermetallic [20]. The bcc iron phase with its diffraction pattern appears clearly on the oxidized precipitate presented in fig. 2. The larger

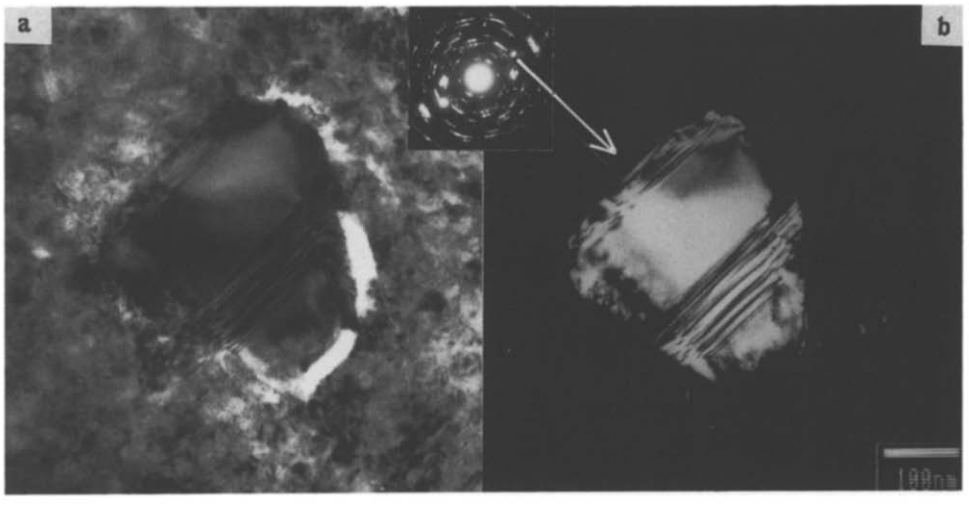

Fig. 3. (a) Unoxidized precipitate located in the bulk of a 1 μm thick oxide layer (at about 0.5 μm from the metallic interface). (b) Dark field of the ⟨10$\bar{1}$3⟩ hcp $Zr(Fe,Cr)_2$ reflection.

oxidized precipitates are observed to have an Fe/Cr ratio of about 0.5 everywhere except on the iron precipitation at the edge. The smaller oxidized precipitates do not show iron precipitation but show a significant iron redistribution: the Fe/Cr ratio at the edge is about 1 while it is decreased to 0.5 in the rest of the precipitate.

– In the middle of the oxide layer, both unoxidized precipitates (i.e. original intermetallic precipitates) with the nominal Fe/Cr ratio of 1.7 and oxidized precipitates with an Fe/Cr ratio decreased to 1.5 are found. One of the unoxidized precipitates is shown in fig. 3. The precipitate is tilted so that the stacking fault contrast characteristic of the Laves phases [17] is ap-

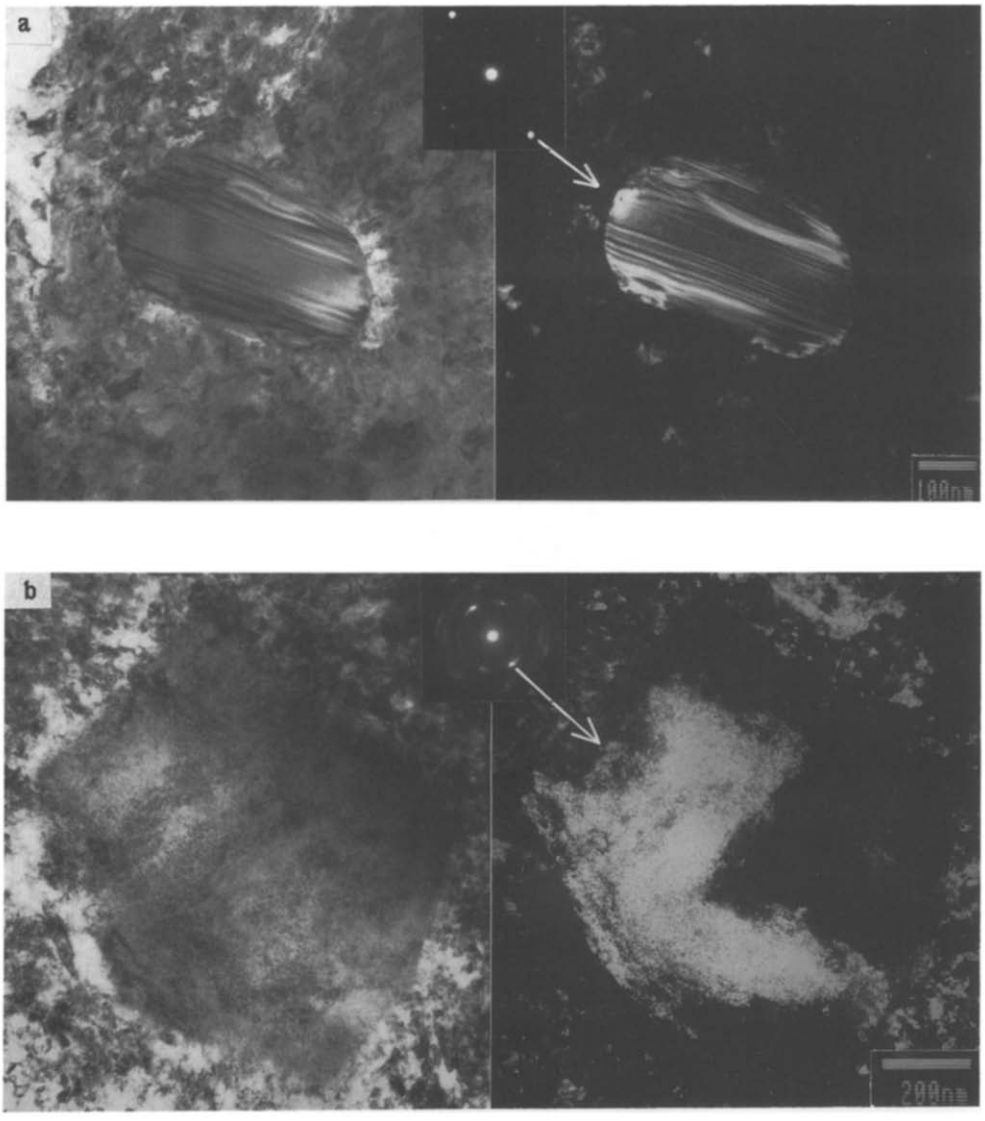

Fig. 4. Various states of the precipitates located in the bulk of a 4 μm thick oxide layer (at about 1 μm from the metallic interface). (a) Unoxidized precipitate. Dark field from a $\langle 10\bar{1}3 \rangle$ hcp $Zr(Fe,Cr)_2$ reflection. (b) Microcrystalline oxidized precipitate- Dark field from a tetragonal ZrO_2 spot. (c) Amorphous precipitate. The first ring of the amorphous diffraction pattern corresponds to a first neighbour distance of 2.8 Å.

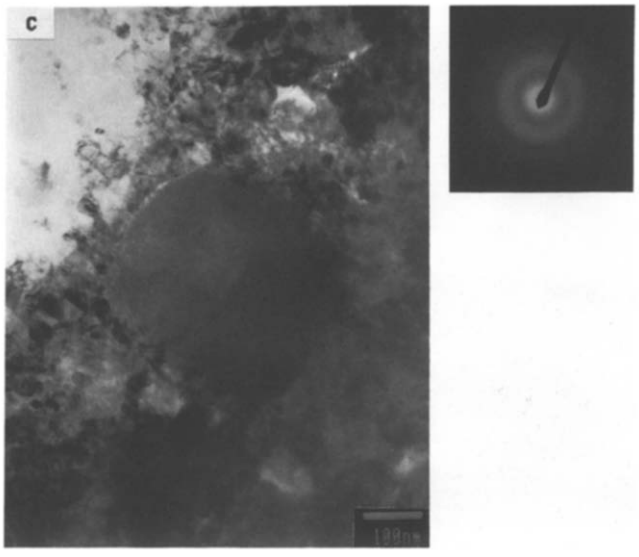

Fig. 4 (continued).

parent. All the unoxidized precipitates observed had a diameter less than 0.35 μm while the oxidized ones covered the whole size distribution (0.15 to 0.8 μm).

3.2.2. 40 day oxidation: oxide thickness = 4 μm (after transition)

At the water–oxide interface of the oxide layer, all the precipitates are oxidized, with an Fe/Cr ratio decreased to about 0.5 as above, except that the iron agglomerates are not visible anymore.

– In a foil taken from the middle of the oxide layer, not only original intermetallic and oxidized precipitates are observed (figs 4a and 4b, respectively) but also amorphous precipitates as evidenced by their diffraction pattern (fig. 4c). These amorphous precipitates, found immersed in the oxide layer, have a characteristic nearest neighbor spacing of 2.8 Å, as measured from the first ring in the diffraction pattern.

As shown in fig. 5, the unoxidized precipitates are small with respect to the oxidized ones. The Fe/Cr ratio of oxidized and amorphous precipitates has decreased to less than 1, and around the largest oxidized precipitates, iron precipitation is occasionally observed.

– At the metal–oxide interface, a large partially oxidized precipitate has also been found (fig. 6). Its oxidized part has an Fe/Cr ratio decreased to 1.3 while in the unoxidized part it remains at 1.7.

3.2.3. 420 day oxidation: oxide thickness = 14 μm

– Both, on the water–oxide interface and in the middle of the oxide layer, all precipitates are oxidized

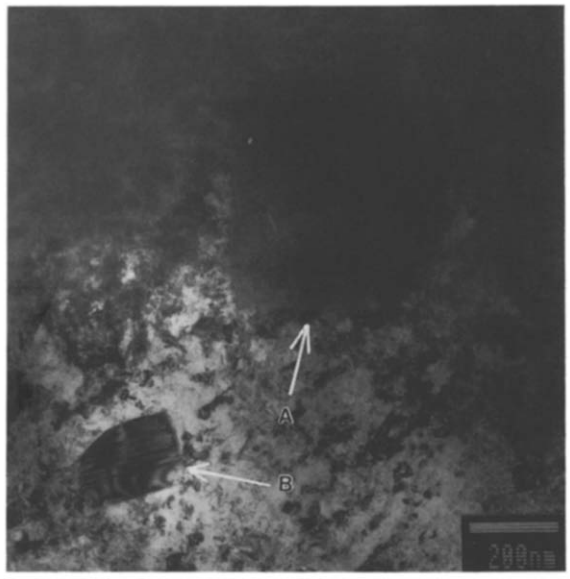

Fig. 5. Large microcrystalline oxidized precipitate (A) near a small unoxidized one (B) located in the bulk of a 4 μm thick oxide layer (at about 1 μm from the metallic interface).

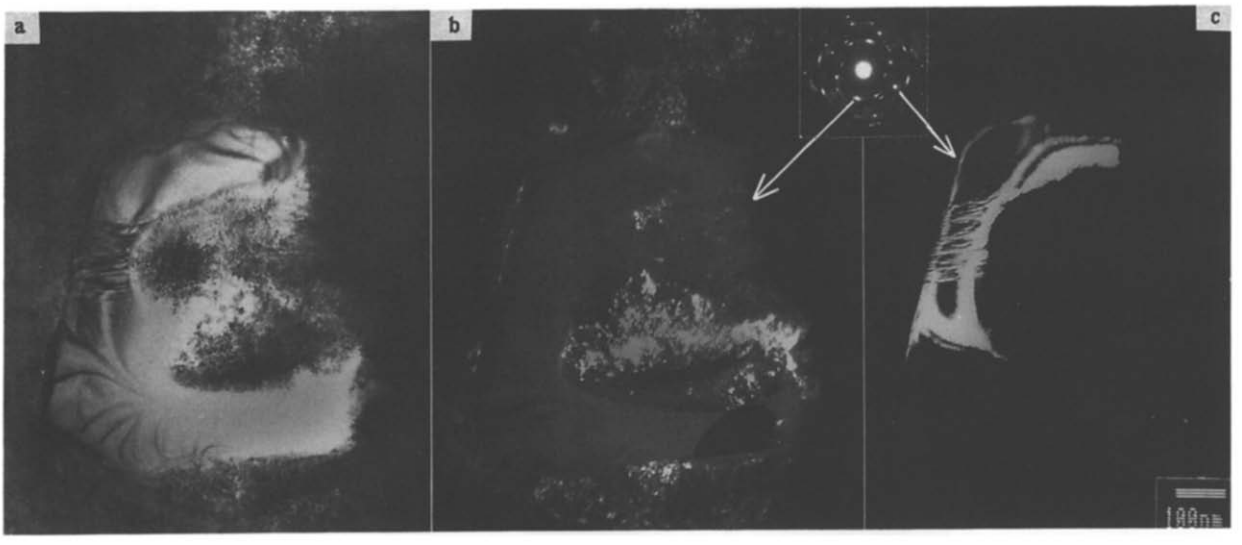

Fig. 6. Large partially microcrystalline oxidized precipitate located at the metal–oxide interface of a 4 μm thick oxide layer. (b) Dark field of a tetragonal ZrO_2 spot. (c) Dark field of a $\langle 10\bar{1}3 \rangle$ hcp $Zr(Fe,Cr)_2$ reflection.

and their Fe/Cr ratio is about 0.5. No iron precipitation can be observed on the precipitates. Near the external surface the iron concentration in the matrix ZrO_2 reaches 1 wt%, but this is thought to be an artefact due to sample contamination in the autoclave.

Since the purpose of the longer oxidation was to follow the precipitate evolution in the porous oxide layer, the metal–oxide interface and the dense oxide layer were not regarded in this case.

3.3. Summary

The above observations are summarized in fig. 7, which shows precipitate morphology as a function of position in the oxide layer.

In fig. 7a, precipitates in the 1 μm oxide layer are shown. Both unoxidized original intermetallic precipitates and oxidized precipitates are present, the smaller precipitates (< 400 nm) having a greater propensitity of being found unoxidized. In the large oxidized precipitates a segregation of iron followed by precipitation is observed.

In fig. 7b, the 4 μm oxide layer is shown. In addition to the previous features, some amorphous precipitates are also seen. After the transition, no iron agglomerates are seen, and the Fe/Cr ratio is low, indicating that iron has been rejected into the matrix.

Only posttransition regions were examined in the oxide at 14 μm shown in fig. 7c. The characteristics of

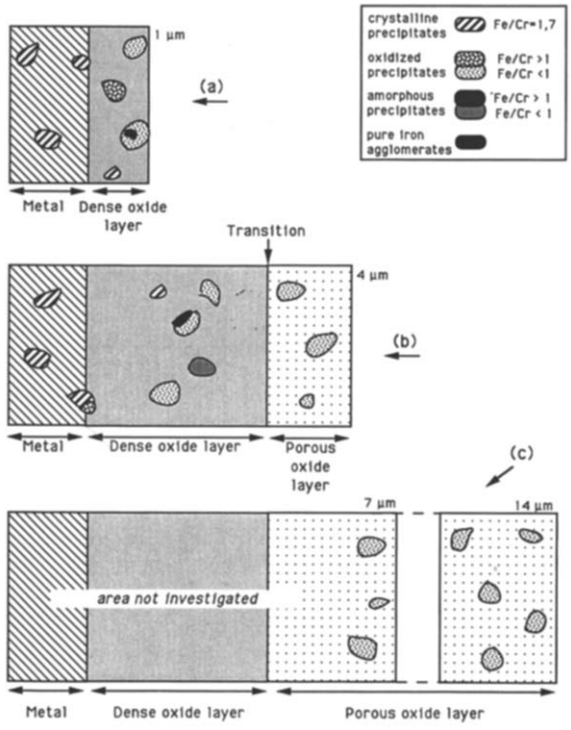

Fig. 7. Schematic view of the various oxidation states of the intermetallic precipitates in the ZrO_2. (a) After 3 day oxidation (1 μm). (b) After 40 day oxidation (4 μm). (c) After 420 day oxidation (14 μm).

the precipitates were quite similar to those observed at the outer surface of the 4 μm oxide, indicating that the precipitates stabilize after the transition.

In all oxidized precipitates the tetragonal/cubic ZrO_2 structure was found.

4. Experimental results on ion irradiated Zircaloy-4

In LWR conditions, intermetallic precipitates undergo a crystalline to amorphous transition and then dissolve. Since their nature has a great impact on the corrosion behaviour of zirconium alloys, the aim of this forthcoming section is to check whether the observations reported above are valid or not for the oxidation of an ion irradiated zirconium alloy.

4.1. Precipitate morphology after irradiation

The ion irradiations were performed on the same reference material as that previously described (sections 2.1 and 3.1). It was verified by transmission electron microscopy (TEM) that the damage conditions reported in section 2.4 amorphize all the precipitates located within a distance of 1 μm from the surface. One of the almost fully amorphous precipitates is shown in fig. 8, along with the ring pattern characteristic of the amorphous phase. The first ring in the amorphous diffraction pattern corresponds to a distance of 2.2 Å, characteristic of the irradiation-made amorphous $Zr(Cr,Fe)_2$ precipitates. By comparison, the irradiated $Zr_2(Ni,Fe)$ precipitates in Zircaloy-2 have an amorphous ring of 2.4 Å. As previously reported [13], precipitate stoichiometry did not change during ion irradiation and amorphization. In summary, ion irradiation induces a structure evolution equivalent to that observed in LWR environment but without any dissolution of the precipitates.

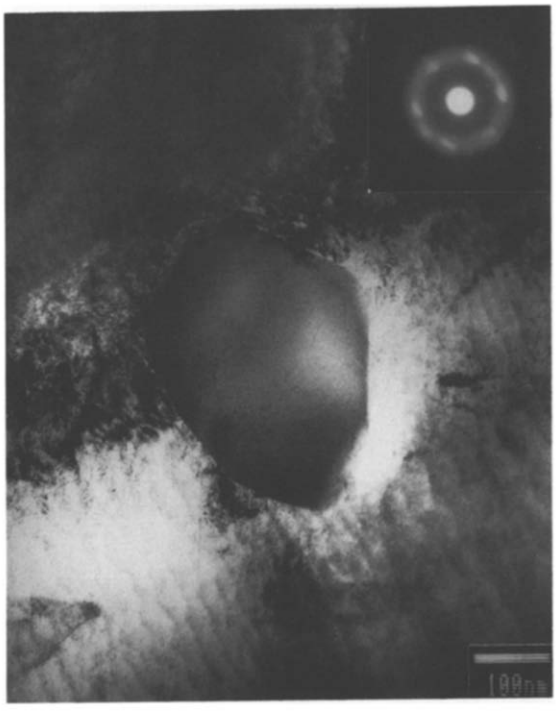

Fig. 8. Amorphous precipitate produced by a 1.5 MeV He^+ irradiation (0.4 dpa/77 K). The first ring of the amorphous diffraction pattern corresponds to a first neighbour distance of 2.2 Å.

4.2. Oxidation of ion irradiated precipitates

3 day oxidation: oxide thickness = 1 μm (before transition). After three days of oxidation, all the depth affected by the irradiation has been oxidized.

– On the external surface and in the middle of the oxide layer, some precipitates remain amorphous and some are oxidized, i.e. microcrystalline with evidence of tetragonal/cubic ZrO_2.

Those precipitates that remain amorphous tend to be small (< 450 nm) and have an Fe/Cr ratio of ~ 0.5 in the precipitate bulk. Interestingly, the first ring of their diffraction pattern corresponds to a first neighbour distance of 2.8 Å. Therefore, while remaining amorphous, their first neighbour distance has increased considerably upon incorporation in the oxide (from 2.2 to 2.8 Å).

Oxidized precipitates have a higher Fe/Cr ratio (1.5) and tend to be larger. They have the same morphology, consisting of small rod-shaped crystallites, a few nm in size, gathered into clusters of similar orientation as that reported above on reference oxidized material.

All the amorphous precipitates and some of the largest oxidized ones show the presence of iron precipitation at the edges. This iron precipitation can take different shapes as shown in fig. 9.

– In small amorphous precipitates, the interface with the zirconium matrix is frequently found coated with precipitated metallic iron (fig. 9a) but agglomeration in a single place like in fig. 9b is also seen.

– In large oxidized precipitates iron is occasionally precipitated, in similar fashion to the reference oxidized precipitates mentioned in section 3.2 even though

in this case the Fe/Cr ratio is still 1.5 in the bulk of the precipitate (fig. 9c).

The precipitates observed in the metal side of the metal–oxide interface show a slight iron depletion at the edges consistent with that measured in the 675 K heat treated samples (Fe/Cr ~ 1.5).

Fig. 10 gives a summary of the above observations. Fig. 10a, illustrates the state of the precipitates after

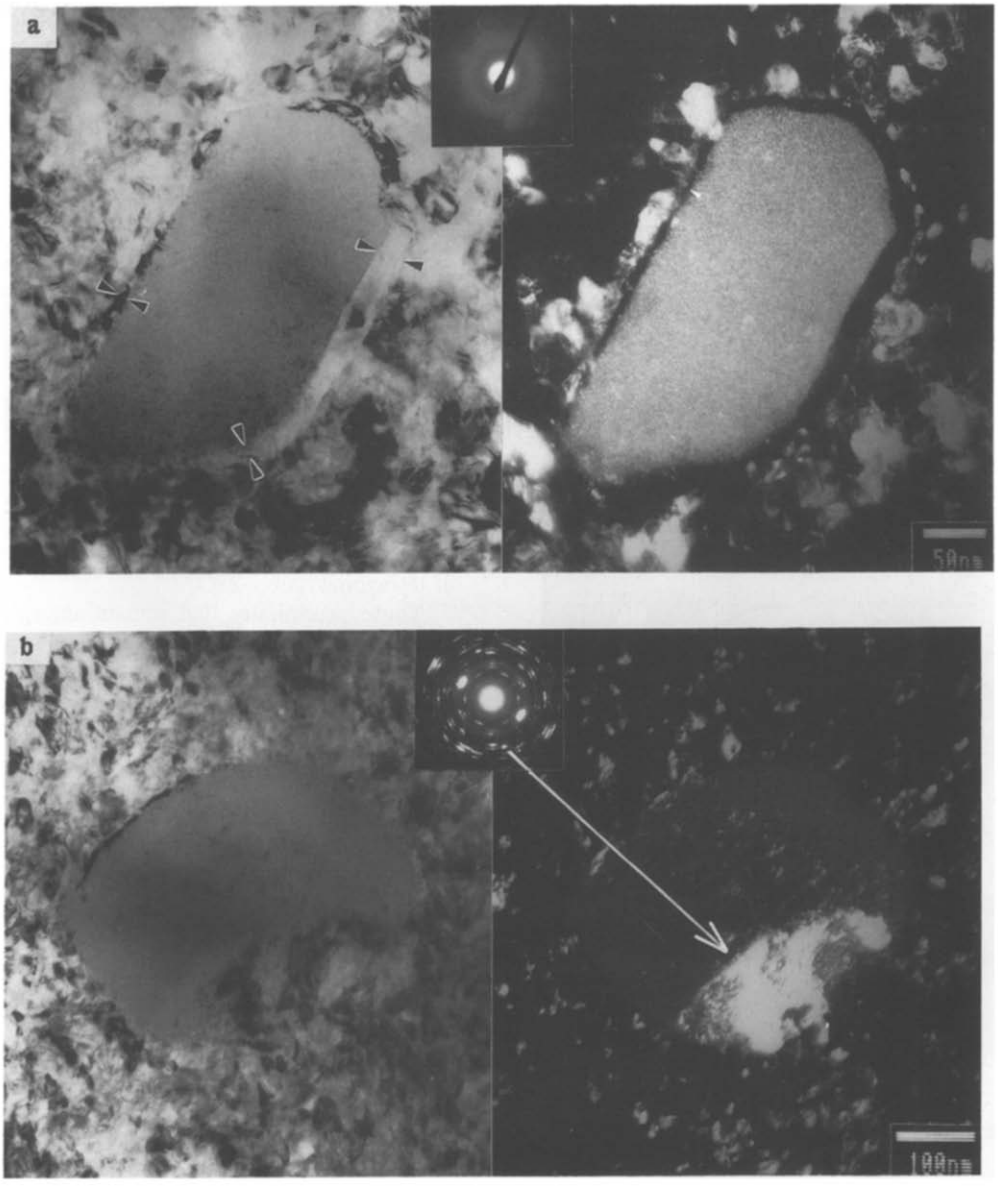

Fig. 9. Behavior of irradiation induced amorphous precipitates during the oxidation process. Precipitates located at the water–oxide interface of a 1 μm thick oxide layer. (a) Remaining amorphous with a thin layer of bcc iron precipitation. (b) Remaining amorphous with a localized iron precipitation. Dark field with a ⟨110⟩ iron reflection. In both cases the first ring of the amorphous diffraction pattern corresponds to a first neighbour distance of 2.8 Å. (c) Oxidizing with precipitation of bcc iron. Dark field with a ⟨110⟩ iron reflection.

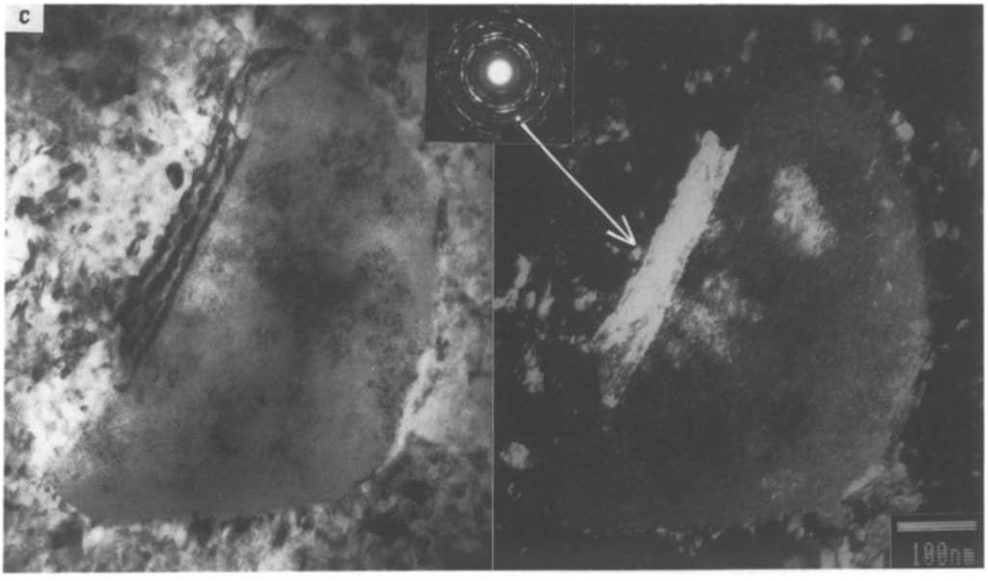

Fig. 9 (continued).

irradiation, and before oxidation. Irradiation produces a 1 μm layer containing only amorphous precipitates. The situation after oxidation is shown in fig. 10b. Near the external surface of the oxide layer, small precipitates are preferentially amorphous with a higher nearest neighbour spacing and a low Fe/Cr ratio (0.5) while large precipitates tends to be oxidized with a higher Fe/Cr ratio (1.5). Closer to the interface with water, iron-coated amorphous precipitates are observed, as well as iron segregation in the large oxidized ones.

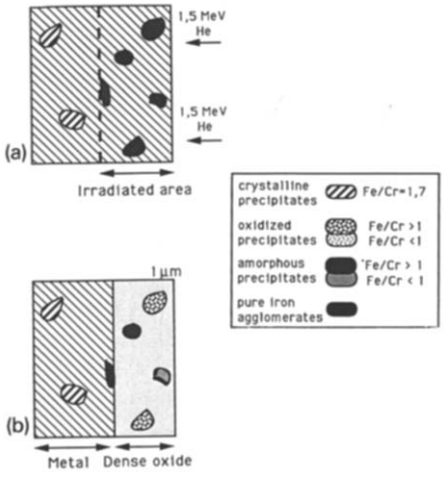

Fig. 10. Schematic view of the state of the intermetallic precipitates. (a) After a 1.5 MeV He^+ irradiation (0.4 dpa/77 K). (b) After the 1.5 MeV He^+ irradiation and 3 day oxidation (1 μm).

4.3. ZrO_2 matrix

Although the primary objective of this work is to investigate precipitate incorporation into the oxide layer, we include here some observations on the oxide layer itself. Our TEM observations agree with work previously published [7,21] in that:

(a) The zirconia crystal structure is predominantly monoclinic, with trace amounts of tetragonal zirconia near the oxide/metal interface.
(b) There is some indication of oxide epitaxy with the base metal. The specific orientation relationships were not identified.
(c) The grain size grows from a few nm at the oxide-metal interface to tens of nm at a distance of about 1 μm from that interface.
(d) In the case of thick ZrO_2 layer (14 μm), fine columnar grains (about 100 nm) aligned in the oxide growth direction are observed at a few μm from the metallic interface.

5. Discussion

The preceding results show that the evolution of the precipitates, while incorporated into the Zircaloy oxide

layer, is a complex process. The oxidation susceptibility of the precipitates, the oxidation state of the constituent elements and the solute element distribution and concentration in the intermetallic precipitates are highly dependent on their position in the oxide layer, as well as on other parameters such as irradiation fluence and precipitate size.

The most important parameters that determine the state of oxidation or solute element depletion of the precipitates appear to be the distance from the metal–oxide interface, roughly equivalent to the residence time in the oxide layer, and the distance from the oxide surface, roughly equivalent to the oxygen potential.

5.1. Reference precipitate oxidation susceptibility

The general trend observed is that $Zr(Fe,Cr)_2$ precipitates are incorporated unoxidized into the oxide layer and are oxidized later. Precipitates that are initially crystalline resist oxidation up to a distance of between 0.5 and 1 μm from the metal–oxide interface. Beyond that thickness, no unoxidized precipitate is found. Their oxidation is therefore delayed compared to that of the zirconium matrix. Other reports have also mentioned that chromium-based intermetallic precipitates in a zirconium matrix oxidize more slowly than the matrix [22,23].

A consistent correlation has also been found between precipitate size and oxidation susceptibility: larger precipitates (> 0.35 μm) oxidize faster than smaller ones do. This is clearly illustrated in fig. 5 where the large precipitate marked A is oxidized while the small precipitate marked B is unoxidized. The largest precipitates (800 nm) oxidize as soon as they cross the metal–oxide interface as observed fig. 6. The reason for this size effect remains unknown.

A specific role of precipitate size in relation to the oxide layer has nevertheless been proposed as part of nodular corrosion enhancement mechanisms, the largest precipitates leading to the highest nodular corrosion rate [24]. The mechanisms considered, however, involve the conduction of electrons through the oxide film by large precipitates and imply that those large precipitates, behaving as cathodes, are therefore less likely to oxidize.

It is interesting to note that in the work of Bradley et al. [23], the only set of samples where precipitates larger than 0.3 μm were present was also the one where an evolution in Fe/Cr ratio was observed. The authors interpreted this observation as an increase in the chromium concentration, but it might be due to a depletion of iron, similar to that observed in the present work. This set of samples also showed the greatest weight gain among the four lots studied.

5.2. Oxidized precipitates morphology and structure

The oxide identified in the oxidized precipitates is tetragonal/cubic ZrO_2. The oxide in the precipitates can be clearly distinguished from that in the matrix, because tetragonal ZrO_2 rings are present whenever the diffraction aperture is located over the precipitate, whereas mainly monoclinic rings appear when the aperture is placed over the matrix. This indicates that the volume fraction of tetragonal ZrO_2 in the oxidized precipitates is higher than in the matrix. It is therefore possible that the alloying elements present in the oxidized precipitates contribute to the stabilization of the tetragonal/cubic phase. This could happen if the alloying elements ionize and dissolve in the ZrO_2 substituting for zirconium and will be discussed later on.

The size and shape of the ZrO_2 crystallites formed in the precipitates are also different from those formed in the matrix. The oxide crystallites from the matrix are spherically shaped, and, except very near the oxide–metal interface where the crystallite size is much smaller, their size is a few tens of nm. The precipitate oxide crystallites are rod-shaped, and smaller in size (a few nm). This morphology is in agreement with the observations of Hannink [25] who reported in bulk ZrO_2 a correlation between small grain size and the presence of tetragonal phase. Diffraction patterns taken from those crystallites show a clear texture in the oxide rings corresponding to preferential orientations of the crystallites, as shown in fig. 4b. Dark fields taken from those preferential directions show that the crystallites arrange themselves in clusters of similar orientation, there existing two or three clusters per precipitate with different orientation. A similar bunching of crystallites into clusters was found by Garzarolli et al. [26].

5.3. Oxidation of alloying elements

The oxygen potential in the oxide layer is controlled by the boundary conditions of Zr oxidation on one side and reduction of water on the other side.

With respect to this oxygen potential gradient, an isothermal cut through Ellingham's diagram indicates that among the elements present in Zircaloy-4, zirconium would oxidize first, followed by chromium and then by iron. It is observed in the present work that these broad thermodynamical tendencies are followed. The oxidation of each alloying element is discussed below in terms of the observed oxidation stages:

5.3.1. Oxidation of the zirconium matrix

It is observed that the zirconium matrix oxidizes first, forming mostly monoclinic zirconia, while the $Zr(Cr,Fe)_2$ precipitates are still unoxidized.

Such a greater stability to oxidation of the $Zr(Cr,Fe)_2$ precipitates with respect to the matrix could be related to the interaction between Zr and the alloying elements into the intermetallic precipitate.

5.3.2. Oxidation of $Zr(Cr,Fe)_2$ precipitates

At a distance between 0.5 and 1 μm from the metal–oxide interface into the oxide layer, the $Zr(Cr,Fe)_2$ precipitates are observed to be oxidized. Since no diffraction spots corresponding to metallic chromium are seen and no chromium segregation nor dissolution is observed, it is possible that chromium is oxidized.

If this is the case, we can assume that it is oxidized into fine Cr_2O_3 since the formation of Cr_2O_3 upon the oxidation of $ZrCr_2$ precipitates in a zirconium matrix has been reported in ref. [22]. The reason why no Cr_2O_3 diffraction spots are seen might be that they cannot be distinguished from those of monoclinic ZrO_2, which is always present to some extent in or around the precipitates.

On the other hand, in those precipitates, a large percentage of tetragonal/cubic ZrO_2 is observed. The prevalence of this tetragonal/cubic ZrO_2 could be due to a strong stabilization effect: chromium, some of which being dissolved substitutionally in the cation lattice of ZrO_2, would play a major role in such a stabilization.

In the dense oxide, iron segregates and precipitates at the precipitate–oxide interface during the oxidation process. Iron precipitation has been observed previously although no metallic bcc iron precipitate was earlier reported; Garzarolli et al. [26] reported that iron agglomerates in oxidized precipitates, so that, depending on the exact location analyzed, the Fe/Cr ratio in the oxidized precipitates varies from 8 to 0.5, in agreement with the present results. Cox and Ploc [27] also noticed that upon oxidation of the bulk intermetallic Zr_3Fe, iron oxidation is preceded by zirconium oxidation and iron segregation.

5.3.3. Oxidation of iron agglomerates

No direct evidence of iron oxidation was found in this work. However, the iron precipitates present in the pre-transition oxide sample are not seen in post-transition ones.

On transition, the oxide becomes porous and the oxygen potential in the oxide layer, at the free surface of the pores, approaches that of reduction of water. The oxidation potential of iron being very close to that of water reduction, it is not surprising that iron oxidizes just after the transition. Cadalbert et al. [28] reported that in a 0.7 μm Zircaloy oxide layer, iron was oxidized only at the outside surface. Since there is some solubility of Fe_2O_3 into ZrO_2 [29], the iron in the agglomerates could then disperse into the ZrO_2 matrix after oxidation. All precipitates observed at the surface of the 4 and 14 μm oxide layers had the same Fe/Cr ratio of 0.5, indicating that the iron concentration in the oxidized precipitates does not evolve after the transition.

It should be interesting to compare the incorporation of $Zr(Cr,Fe)_2$ precipitates with that of $Zr_2(Ni,Fe)$ precipitates present in Zircaloy-2. Due to the fact that the oxygen potential for oxidation of nickel is higher than that for reduction of water, we expect that nickel will survive unoxidized in the porous oxide scale, as observed by Ploc and Cox [27].

5.4. Amorphous precipitates in the oxide layer

In addition to the microcrystalline oxidized precipitates, amorphous precipitates were also found in oxide layers. These precipitates are not artifacts of sample preparation as in ref. [30], because they are found not only at the foil edge but in the thicker regions as well.

Similar observations of amorphous precipitates in an unirradiated oxide layer were reported by Bradley et al. [23] and Tanaka [8]. Garzarolli et al. later suggested that the amorphous precipitates observed were actually microcrystalline [26]. The present observations confirm that they are amorphous, rather than microcrystalline, because:

(a) the precipitates are completely featureless in bright field, and no change in contrast happens upon tilting.
(b) their diffraction pattern shows only one diffuse ring, instead of several sharp rings, as expected from a microcrystalline oxide.

It is not clear what is the driving force for this amorphization. For other zirconium compounds an hydrogen intake has been proposed as a possible driving force [31,32]. Such a hypothesis, in our case, would be consistent with the fact that, when embedded in the oxide, these amorphous precipitates exhibit a first ring in their diffraction pattern corresponding to a nearest neighbour spacing of 2.8 Å. This spacing is to be compared to the corresponding spacing of 2.2 Å measured in $Zr(Cr,Fe)_2$ precipitates amorphized by electron, ion or neutron irradiations [33]: The amorphiza-

tion of the precipitates in the oxide layer produces a significant increase of the first neighbour spacing. The reason for such a dilation could be the absorption of either hydrogen or oxygen into the lattice. In the latter case, there would then be two steps of reaction upon incorporation into the oxide layer: one resulting in an amorphous oxidized precipitate as in fig. 4c and the other in a microcrystalline oxidized precipitate such as shown in fig. 4b.

5.5. *Oxidation of irradiated amorphous precipitates*

The irradiated amorphous precipitates and the reference precipitates show the same oxidation susceptibility since after a 3 day oxidation test, all irradiated amorphous precipitates have undergone a structural evolution:

- Some oxidize, getting a morphology completely identical to that of the oxidized reference precipitates.
- Some remain amorphous upon incorporation into the oxide layer, but their first neighbour spacing increases from 2.2 to 2.8 Å making them completely equivalent to the amorphous precipitates observed in the oxidized reference material.

As proposed in the case of reference material, there would be, in the case of irradiated material also, two forms of reaction upon incorporation into the oxide layer, one resulting in an amorphous precipitate with a nearest neighbour spacing increased from 2.2 to 2.8 Å, and the other in a microcrystalline oxidized precipitate, the small precipitates being more prone to the first reaction.

The qualitative evolution of alloying elements in the case of irradiated amorphous precipitates is similar to that observed in the case of reference precipitates. Upon incorporation, chromium remains distributed homogeneously while iron is depleted from the precipitates, as well as redistributed internally. The discussion proposed above for the chromium evolution in oxidized reference precipitates is then still valid, that is, most of it could be oxidized as very fine Cr_2O_3, with a small quantity dissolved in the zirconia, stabilizing the tetragonal/cubic phase.

There are, however, two important differences for iron. First, in the irradiated samples segregation and precipitation of iron is observed in microcrystalline oxidized precipitates as well as in amorphous ones. On the other hand, the iron depletion is much higher in the microcrystalline oxidized precipitates observed in the reference sample than in the irradiated one with, respectively, a Fe/Cr ratio of 0.5 and 1.5.

6. Consequences for Zircaloy-4 oxidation

This work indicates that most of the precipitates in Zircaloy oxidize later than the matrix and that upon oxidation, an iron redistribution in the precipitate followed by an iron redissolution in the matrix occurs. Such effects could modify the properties of the oxide in several ways, such as stabilizing the tetragonal/cubic phase, or changing the conduction properties of the oxide.

After three days in the autoclave, no compelling evidence was seen of an effect of precipitate amorphization on oxidation rates since the weight gain of ion irradiated Zircaloy-4 was only about 10% smaller than the reference case. This difference which could be due to experimental variations needs to be confirmed. Such testing is currently in progress.

It is worth noting that Etoh [34] found a tenfold reduction in corrosion rate and suppression of nodular corrosion during oxidation of Zircaloy-2 irradiated at fluences up to 7×10^{24} n m^{-2}, compared to unirradiated Zircaloy-2. The authors attributed this effect to the larger quantity of iron and chromium dissolved in the matrix upon neutron irradiation. This could be the reason for which no significant effect of ion irradiation is seen in the present work since in the ion irradiated samples there is no iron and chromium redissolution.

7. Conclusions

In this work, TEM examinations of reference Zircaloy-4 oxide layers of different thicknesses are presented. The aim of this characterization was to understand the mode of incorporation of intermetallic precipitates in the oxide layer and to discuss their possible role in the oxidation process.

In order to investigate a possible role of irradiation induced amorphization on oxidation, ion irradiated Zircaloy-4 samples have also been studied.

The main experimental observations are the followings:

- Reference intermetallic and irradiated amorphous precipitates oxidize more slowly than the matrix and are embedded unoxidized by the ZrO_2 oxidation front. The oxidation processes of irradiated and unirradiated precipitates are similar.
- Both reference intermetallic and irradiated amorphous precipitates seem to exhibit two forms of reaction during the oxide layer growth, one resulting in an oxidized microcrystalline structure and one resulting in an amorphous structure with a nearest neighbour spac-

ing of 2.8 Å, the smallest precipitates being more prone to the second.

– The oxide found in the oxidized microcrystalline precipitate is ZrO_2 with a higher proportion of tetragonal/cubic zirconia than in the matrix. In the amorphous precipitates the nearest neighbour spacing of 2.8 Å, larger than that measured on irradiated amorphous precipitates ($d = 2.2$ Å) suggests a possible absorption of oxygen or hydrogen into the precipitate upon incorporation into the oxide layer.

– In the precipitates iron concentration evolves considerably upon both forms of oxidation, especially before the transition. A segregation of iron to the precipitate–matrix interface is observed in the case of microcrystalline oxidized precipitates and in the case of irradiated-amorphous and oxidized precipitates ($d =$ 2.8 Å). In some cases, a precipitation of metallic bcc iron is observed. After the transition iron precipitates are not observed anymore suggesting that they are dissolved in the ZrO_2 matrix. The iron redissolution into the matrix seems to be delayed in the case of irradiated precipitates.

Acknowledgements

The authors would like to thank F. Gomez for his expert sample preparation, to M. Dubus for his help with the ion irradiations and to C. Regnard and P. Desré for stimulating discussions.

D. Pêcheur was partially supported by Fragema-Framatome Combustible and Cézus in the framework of a joint thesis research contract with CEA.

References

[1] D.G. Franklin and P.M. Lang, Proc. 9th Int. Symp. on Zirconium in the Nuclear Industry, Kobe, Japan, November 1990, ASTM-STP 1132 (1991) 3.

[2] A.A. Strasser and M.G. Andrews, Proc. IAEA Technical Committe Meeting on Fundamental Aspects of Corrosion of Zirconium Base Alloys in Water Reactor Environments, Portland, September 1989 (IAEA, Vienna, 1990) IWGFPT/34, ISSN 1011-2766.

[3] F. Garzarolli and H. Stehle, Proc. IAEA Int. Symp. on Improvements in Water Reactor Technology and Utilization, Stockholm, September 1986, IAEA SM-288-24.

[4] J. Godlewski, Thèse, Univ. Tech. de Compiegne (1990).

[5] F. Garzarolli, E. Steinberg and H.G. Weidinger, 8th Int. Symp. on Zirconium in the Nuclear Industry, San Diego, June 1988, ASTM-STP 1023 (1989) 202.

[6] C.M. Eucken, P.T. Finden, S. Trapp-Pritsching and H.G. Weidinger, Proc. 8th Int. Symp. on Zirconium in Nuclear Industry, San Diego, June 1988, ASTM-STP 1023 (1989) 113.

[7] J. Godlewski, J.P. Gros, M. Lambertin, J.F. Wadier and H. Weidinger, Proc. 9th Int. Symp. on Zirconium in the Nuclear Industry, Kobe, Japan, November 1990, ASTM-STP 1132 (1991) 416.

[8] M. Tanaka, (Pechiney, Voreppe) private communication.

[9] R. Tricot, Rev. Gén. Nucléaire (January 1990) pp. 8–23.

[10] R.W. Gilbert, M. Griffiths and G.J.C. Carpenter, J. Nucl. Mater. 135 (1985) 265.

[11] W.S. Yang, R.P. Tucker, B. Cheng and R.B. Adamson, J. Nucl. Mater. 138 (1986) 185.

[12] ASTM Standard Practice for Neutron Irradiation Damage Simulation by Charged Particle Irradiation, E521/83.

[13] F. Lefebvre and C. Lemaignan, J. Nucl. Mater. 165 (1989) 122.

[14] J.F. Ziegler, J.P. Biersack and U. Littmark, The Stopping and Range of Ions in Matter, vol. 1, ed. J.F. Ziegler (Pergamon, New York, 1985).

[15] W.S. Yang, EPRI report NP-5591 (1988).

[16] M. Griffiths, R.W. Gilbert and G.J.C. Carpenter, J. Nucl. Mater. 150 (1987) 53.

[17] P. Chemelle, D.B. Knorr, J.B. Vandersande and R.M. Pelloux, J. Nucl. Mater 113 (1983) 58.

[18] X.Y. Meng and D.O. Northwood, J. Nucl. Mater. 132 (1985) 80.

[19] D. Charquet and E. Alheritiere, Workshop on Second Phase Particles and Matrix Properties in Zircaloys, Erlangen, Germany, July 1985.

[20] R.A. Ploc, Proc. 8th Int. Symp. on Zirconium in the Nuclear Industry, San Diego, June 1988, ASTM--STP 1023 (1989) 498.

[21] R.A. Ploc, J. Nucl. Mater. 28 (1968) 48.

[22] B. De Gelas, G. Beranger and P. Lacombe, J. Nucl. Mater. 28 (1968) 185.

[23] E.R. Bradley and R.A. Perkins, Proc. IAEA Technical Committe Meeting on Fundamental Aspects of Corrosion of Zirconium Base Alloys in Water Reactor Environments, Portland, September 1989 (IAEA, Vienna, 1990) IWGFPT/34, ISSN 1011-2766.

[24] R. Ramasubramanian, Proc. IAEA Technical Committe Meeting on Fundamental Aspects of Corrosion on Zirconium Base Alloys in Water Reactor Environments, Portland, September 1989 (IAEA, Vienna, 1990) IWGFPT/34, ISSN 1011–2766.

[25] R.H.J. Hannink, K.A. Johnston, R.T. Pascoe and R.C. Garvie, in: Science and Technology of Zirconia, Advances in Ceramics, vol. 3, eds. A.H. Heuer and L.W. Hobbs (The American Ceramic Society, Columbus, OH, 1981).

[26] F. Garzarolli, H. Seidel, R. Tricot and J.P. Gros, Proc. 9th Int. Symp. on Zirconium in the Nuclear Industry, Kobe, Japan, November 1990, ASTM-STP 1132 (1991) 395.

[27] R.A. Ploc and B. Cox, Workshop on Second Phase Parti-

cles and Matrix Properties in Zircaloys, Erlangen, Germany, July 1985.
[28] R. Cadalbert, L. Boulanger, G. Brun, S. Lansiart, G. Silvestre and P. Juliet, Proc. Int. Topical Meeting on LWR Fuel Performance, Avignon, April 1991, p. 784.
[29] R.W. Wilhelm Jr. and D.S. Howarth, Ceram. Bull. 58 (1979) 228.
[30] D. Pêcheur, A.T. Motta and C. Lemaignan, J. Nucl. Mater., submitted.
[31] W.J. Meng, P.R. Okamoto, L.J. Thompson, B.J. Kestel and L.E. Rehn, Appl. Phys. Lett. 53 (1988) 1820.
[32] J.Y. Lee, W.C. Choi, Y.G. Kim and J.Y. Lee, Acta Metall. Mater. 39 (1991) 1693.
[33] A.T. Motta, F. Lefebvre and C. Lemaignan, Proc. 9th Int. Symp. on Zirconium in the Nuclear Industry, Kobe, Japan, November 1990, ASTM-STP 1132 (1991) 718.
[34] Y. Etoh, K. Kikuchi, T. Yasuda, S. Koizumi, M. Oishi, Proc. Int. Topical Meeting on LWR Fuel Performance, Avignon, April 1991, pp. 691–700.